

# Fabrication of coronagraph masks and laboratory scale star-shade masks: characteristics, defects and performance

Kunjithapatham Balasubramanian, A.J. Eldorado Riggs, Eric Cady, Victor White, Karl Yee, Daniel Wilson, Pierre Echternach, Rich Muller, Camilo Mejia Prada, Byoung-Joon Seo, Fang Shi, Daniel Ryan, Santos Fregoso, Jacob Metzman, and Robert Casey Wilson  
Jet Propulsion Laboratory, California Institute of Technology  
4800 Oak Grove Drive, Pasadena, CA 91109  
kbala@jpl.nasa.gov Tel: 818-393-0258

## ABSTRACT

NASA WFIRST mission has planned to include a coronagraph instrument to find and characterize exoplanets. Masks are needed to suppress the host star light to better than  $10^{-8} - 10^{-9}$  level contrast over a broad bandwidth to enable the coronagraph mission objectives. Such masks for high contrast coronagraphic imaging require various fabrication technologies to meet a wide range of specifications, including precise shapes, micron scale island features, ultra-low reflectivity regions, uniformity, wave front quality, etc. We present the technologies employed at JPL to produce these pupil plane and image plane coronagraph masks, and lab-scale external occulter masks, highlighting accomplishments from the high contrast imaging testbed (HCIT) at JPL and from the high contrast imaging lab (HCIL) at Princeton University. Inherent systematic and random errors in fabrication and their impact on coronagraph performance are discussed with model predictions and measurements.

Key words: WFIRST, Coronagraph, Shaped pupil masks, Hybrid Lyot masks, HCIT, star-shade occulter

## 1. INTRODUCTION

The WFIRST Coronagraph Instrument (CGI) is designed to operate with two kinds of masks (Krist, *et al.*, 2016) to suppress host star light to the level of  $10^{-8} - 10^{-9}$  contrast over a chosen region of the image plane and spectral band to observe and characterize exoplanets in the visible to near IR spectral region. Hybrid Lyot Coronagraph (HLC) masks (Trauger, *et al.*, 2016) are designed to operate in the focal plane to diffract star light to a subsequent Lyot stop. These masks are designed with a profiled dielectric layer on top of a metal layer to handle both amplitude and phase effectively to suppress on axis star light. Similarly, the Shaped Pupil Coronagraph (SPC) masks (Zimmerman, *et al.*, 2016, Cady, *et al.*, 2016) which operate in the pupil plane to shape/apodize the pupil amplitude are made with highly absorbing black silicon structures in a highly reflective background. These masks contain isolated island features and hence are designed to operate in reflective mode to avoid a transmissive substrate that can cause dispersion induced performance impact. Starshade occulters (Cash, 2006, Crill and Siegler, 2017) on the other hand operate far off outside the telescope diffracting and suppressing the star light as it enters the telescope. For practical experimental validation of the concepts in the lab (Cady, *et al.*, 2009, Sirbu, *et al.*, 2016, Galvin, *et al.*, 2016) miniaturized versions of these star-shade masks are designed and fabricated on silicon wafers with precisely shaped petals with sub micron edge accuracy. All of these masks present significant challenges in fabrication due to the level of accuracy needed with minimum defects. We discuss here the fabrication and practical accomplishments in relation to performance of each of these devices. Details of the testbed, methodologies and results can be found in companion papers in this SPIE proceedings volume.

---

\*kbala@jpl.nasa.gov; phone 1 818 393-0258

The architecture of the two coronagraph modes on our high contrast imaging testbed (HCIT) is shown in the conceptual diagram in figure 1. The shaped pupil coronagraph (SPC) architecture consists of a reflective shaped pupil mask (SPM), a focal plane mask (FPM) and a Lyot stop (LS). The Hybrid Lyot architecture consists of a transmissive focal plane mask, a lyot stop and field stop (FS) besides two deformable mirrors. Additionally the FPMs incorporate a Zernike phase dimple at the center of the mask for enabling low order wavefront sensing (LOWFS) and control as illustrated in the conceptual schematic (Shi, *et al.*, 2016, 2017). The SPMs provide a “dark hole” in the image plane that covers a “bow tie” shaped region where star light suppression is achieved for planet observation and characterization. To observe over a 360 deg region, three such masks are designed and fabricated. The SPC architecture is also designed to incorporate another reflective SPM for disc science observations over 360 degree, but with a larger inner working angle. The HLC masks serve a 10% bandwidth of the spectral band and hence two different masks are designed to cover the two primary spectral bands of interest. The various masks and the required wavelength bands are shown in figure 2.

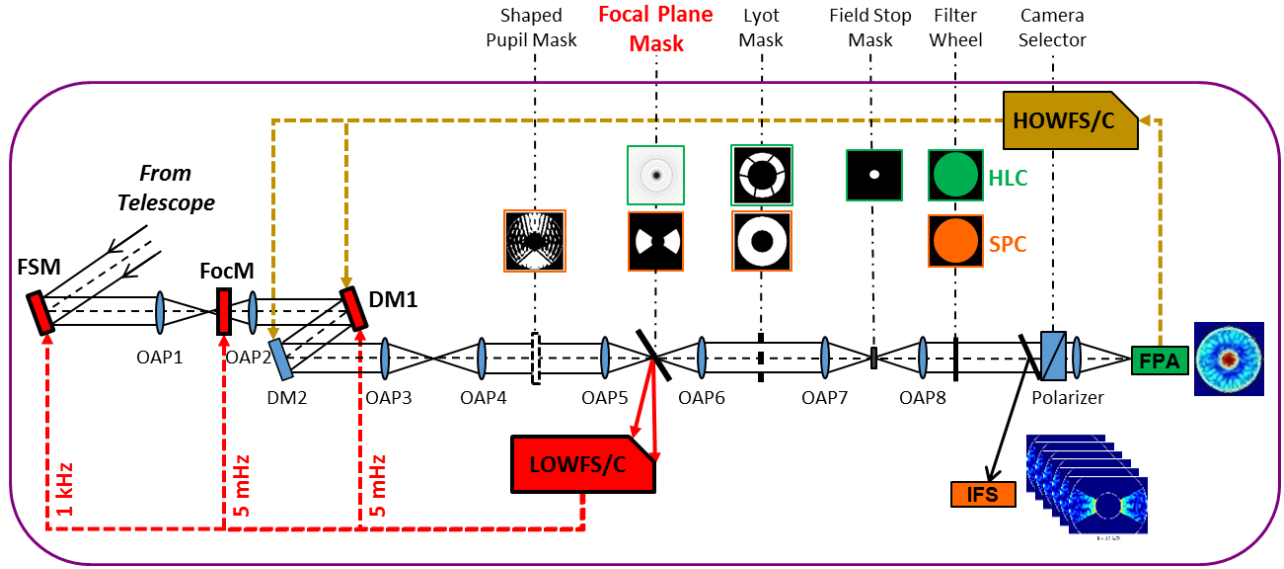


Figure 1. Conceptual schematic of the coronagraph testbed showing the SPC, HLC and LOWFS architectures (Shi, *et al.*, 2017)

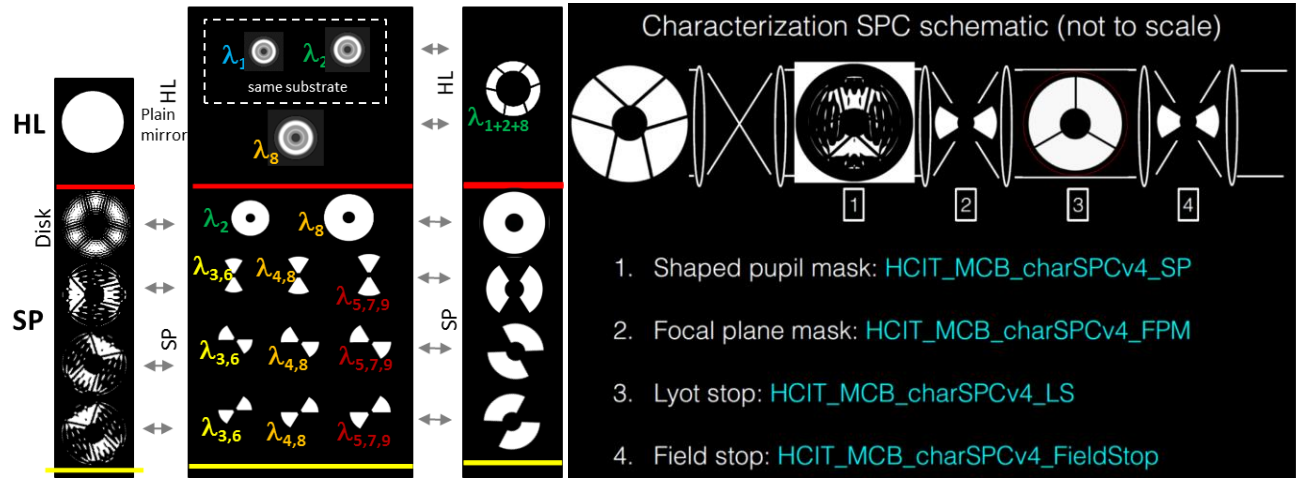


Figure 2. Various masks needed for SPC and HLC modes.  $\lambda_1=506\text{nm}$ ,  $\lambda_2=575\text{nm}$ ,  $\lambda_3=660\text{nm}$ ,  $\lambda_4=770\text{nm}$ ,  $\lambda_5=890\text{nm}$ ,  $\lambda_6=661\text{nm}$ ,  $\lambda_7=883\text{nm}$ ,  $\lambda_8=721\text{nm}$ ,  $\lambda_9=940\text{nm}$

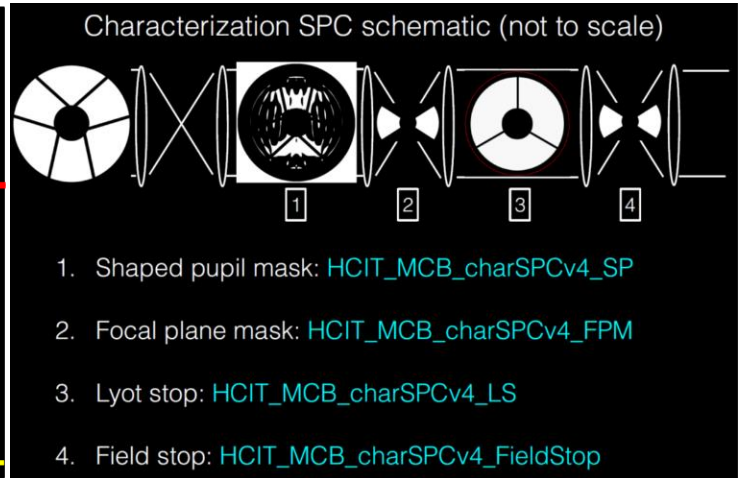


Figure 3. An SPC mask and associated FPM and LS masks schematic design concept. (courtesy: Neil Zimmerman, Space Telescope Science Institute)

## 2. FABRICATION TECHNOLOGIES

The fabrication of the various masks depends critically on the type of masks and their features. Table 1 below lists the broad categories of masks and the appropriate fabrication technologies (Balasubramanian, *et al.*, 2013) adopted for them. Each mask type involves multiple processes with precision controls at each stage to minimize defects and imperfections.

Architecture	Masks / Types	Basic Design	Technologies
Shaped Pupil Coronagraph (SPC)	Reflective Shaped Pupil Masks for Discovery, Spectroscopy, Disk Science Different Orientations Lyot Stops Focal Plane Masks / Field Stops as needed	SPMs - Black silicon features on a reflective background with ideally binary structures  Lyot Stops and Field Stops - Apertures etched on thin silicon-on-insulator (SOI) wafer with thin membrane edges	Electron Beam Lithography (EBL) Cryogenic Reactive Ion Etching (CRIE) Deep Reactive Ion Etching (DRIE) Metal coating in UHV chamber
Hybrid Lyot Coronagraph (HLC)	Transmissive HLC FPM for different spectral bands FPM with LOWFS Phase Dimple Lyot Stops Field Stops	Profiled dielectric on metal with phase dimple for LOWFS on anti reflection (AR) coated fused silica substrate  Lyot Stops and Field Stops - Apertures etched on thin silicon wafer	Electron Beam Lithography (EBL) Gray scale etching  Metal coating in UHV chamber
Lab-scale Star-shade mask	Transmissive petal shaped apertures	Precision edges of petal shaped apertures on a thin silicon nitride membrane on a Silicon-on-insulator (SOI) wafer	Electron Beam Lithography (EBL) Anisotropic Deep Reactive Ion Etching (DRIE) Isotropic Etching Metal coating in UHV chamber

Table 1. Various masks and fabrication technologies

## 3. SHAPED PUPIL MASKS

### Reflective SPLC mask designs

Shaped pupil masks are designed as binary reflective structures with ideally 1 and 0 specular reflectance on adjacent pixels on the surface of a highly polished silicon substrate. The reflective regions are of aluminum coating and absorptive regions are made of black silicon surface. The 1 and 0 features are generally designed with 1000x1000 pixels or 2000x2000 pixels optimized to absorb and/or diffract star light outside of the chosen region in the subsequent focal plane. The Lyot stop helps to block off unwanted diffracted light from the on axis star without significantly affecting the off axis planet light. The planet throughput and star light suppression are primary merit factors in the design of the mask which are discussed in a companion paper (Riggs, *et al.*, 2017) in this proceedings volume. The design concept is illustrated in figure 3.

### Fabrication

The shaped pupil mask is fabricated on a 4mm thick 100 mm dia silicon blank polished to  $\lambda/20$  rms flatness. The wafer is first coated with ~170nm thick aluminum in an ultra high vacuum chamber by electron beam evaporation and then coated with a photoresist. The mask patterns per design is first recorded by electron lithography on a large glass master which is then transferred onto the silicon disc as shown in figure 4 by contact lithography process (Balasubramanian, *et al.*, 2013, 2016). Then the exposed photoresist on aluminum is etched away opening the pattern to

be blackened by cryogenic deep reactive ion etching of silicon. After cryo etching of black silicon regions, the silicon disc is diced off to obtain the 35mmx35mm square masks which are then thoroughly cleaned and dried. The masks are then

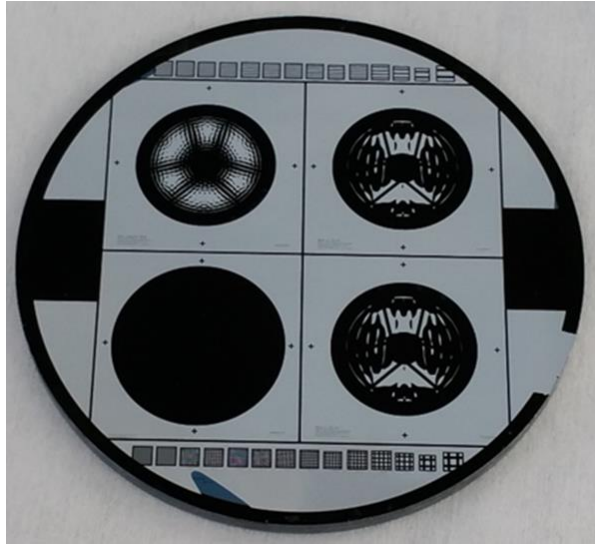


Figure 4. Aluminum coated silicon blank patterned with 3 masks inside 35mmx35mm squares and a large black circle for characterization.



Figure 5. A fabricated SPC characterization mask with 1000 x 1000 pixels design with a 3mm wide black buffer zone around. Pupil diameter for this design is 19.7mm.

characterized microscopically. A composite image of the entire mask is assembled with about 300 sub images obtained with a scanning microscope. One such composite image of a mask made in 2015 is shown in figure 5. Also, several individual images are taken at higher resolution to identify defects and quantify them for later performance modeling.

### Identification of defects and imperfections

One of the key goals in the fabrication of masks for the testbed is to identify the defects and compare with the design specs. Detailed images enable modeling the performance as also to pick the best mask for installation in the testbed for detailed end to end tests. Important characteristics to observe and measure are:

- 1) minimum physical feature size and shape
- 2) defects in black and white regions
- 3) total hemispherical reflectivity of the black silicon structures
- 4) specular reflectivity of black silicon
- 5) specular reflectivity of metal regions
- 6) surface finish of the mask as measured interferometrically

Figure 6 shows the small features on the mask with measurements. The pixel width is  $\sim 19.7 \mu\text{m}$  as measured with a 50x 0.55NA objective and as expected per design. The minimum feature size is within  $\pm 0.5 \mu\text{m}$  of design specs over the entire mask. The corners of the connected pixel edges are also within  $\pm 0.5 \mu\text{m}$  as seen. Due to the lithographic bias typical of contact lithography and also due to diffraction at the edges of these small features, one can see rounded corners of pixels in figure 7. However these small imperfections do not affect the performance in the testbed as system level tests demonstrated (Cady, *et al.*, 2017). Another type of defects seen on the aluminum

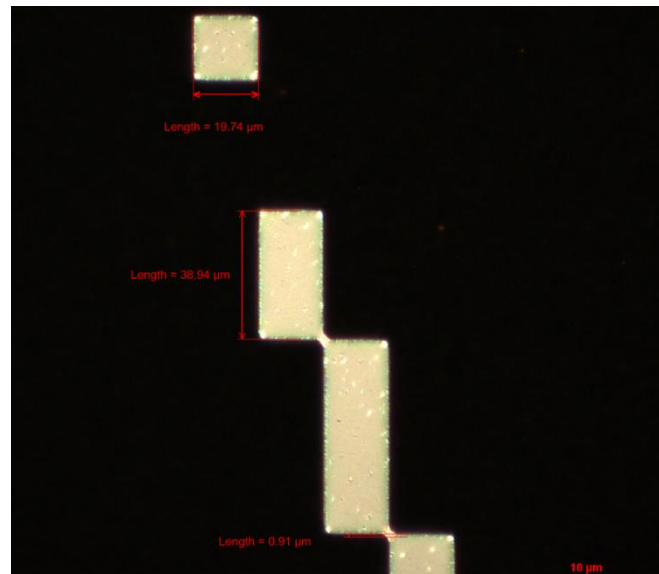


Figure 6. Microscopic image of pixels on the mask shown in figure 5. Minimum feature size is  $19.7 \mu\text{m}$

regions where micron scale imperfections appear as in figure 7. This is caused by the various chemical and ion based processes that the sensitive Aluminum surface goes through. Several modifications to the processes and control of sequences and durations have resulted in much better surfaces in subsequent runs.

Figures 8 and 9 show a remarkably clean aluminum surface on a more recent fabrication. Feature shape accuracy is also within  $\pm 0.5\mu\text{m}$ . We also examined the features and surface with scanning electron microscopy (SEM). Figure 10 shows the SEM images at two different magnifications. Clean aluminum pixels are seen as pads above the “grassy” silicon surface around them. The 5000x magnified SEM image shows the sub micron needle structures of black silicon that absorb the incident light. The conductivity of silicon is chosen to be very low with appropriate doping to increase the absorption thus providing very low specular and diffuse reflectivity. Measured results are shown in section 3 below. Aluminum reflectivity is typically  $\sim 90\%$  in the visible except at around 800nm where a native absorption dip occurs. Black silicon surface is typically very dark with diffuse hemispherical reflectance  $\sim 0.1\%$  and  $<10^{-7}$  specular reflectance which are significantly below the level needed for coronagraph performance as demonstrated with testbed results.



Figure 7. Microscopic image of pixels on the mask shown in figure 5. Systematic rounded corners of the pixels and a number of micron scale surface imperfections on the aluminum surface are seen here.

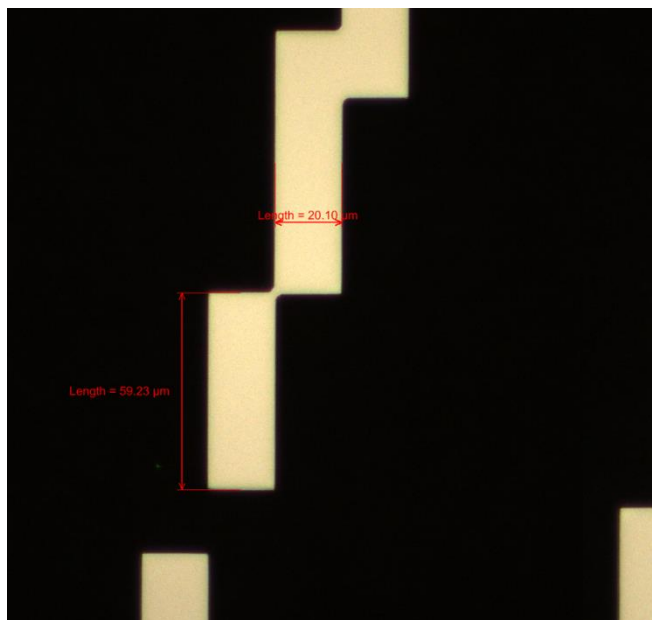


Figure 8. Microscopic image of pixels on the mask fabricated subsequently after process improvements.

Focal plane and Lyot stop masks for SPC architecture are fabricated on silicon-on-insulator (SOI) wafers (Ref: Balasubramanian *et al.*, 2016) as shown in figure 11. Multiple copies of the same device along with variations of physical dimensions are made on the same wafer for redundancy and to choose the best ones.

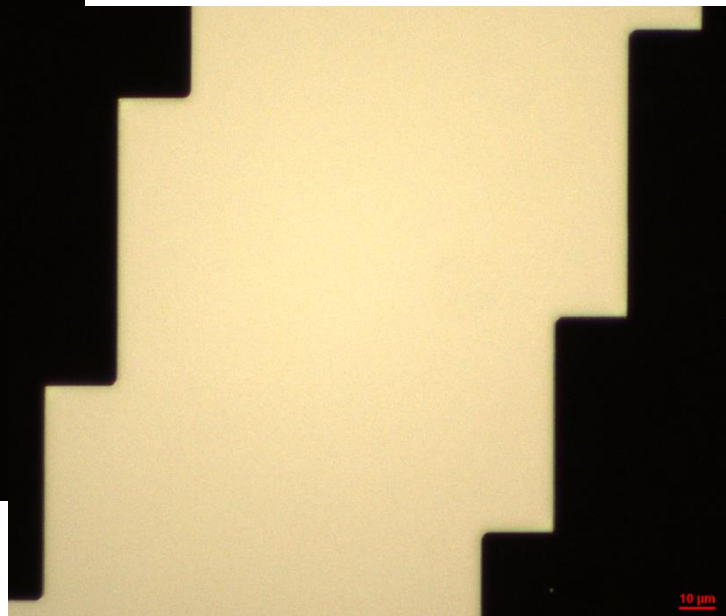


Figure 9. Microscopic image of aluminum regions on the mask fabricated subsequently after process improvements. Micron scale surface imperfections seen in previous runs are not observed on this image.



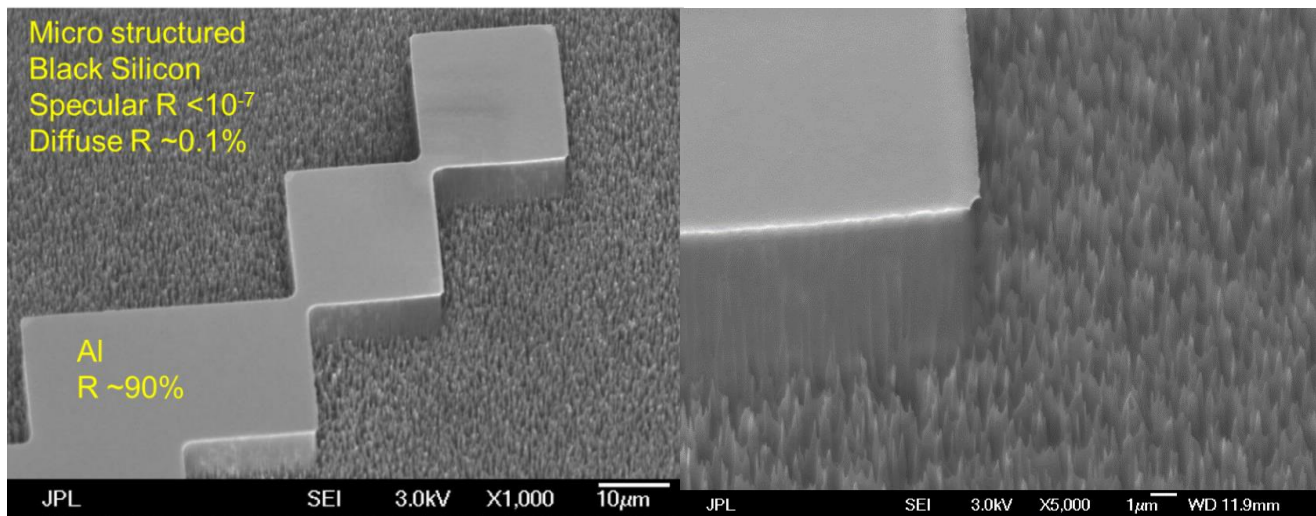


Figure 10. SEM images of the shaped pupil mask on silicon showing the highly reflective metal features and the highly absorbing black silicon surface. The image on the right shows a metal pad corner on the left image at 5000x magnification.

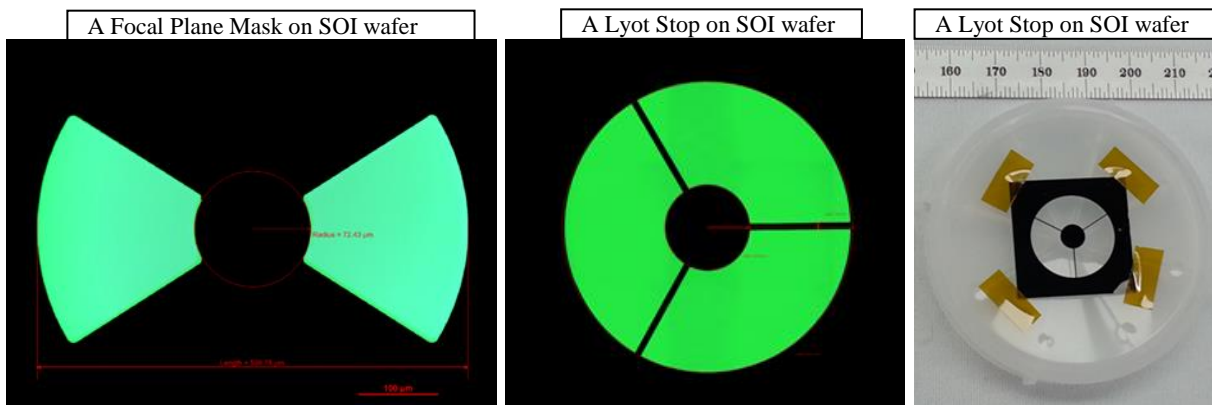


Figure 11. Microscopic image in transmission of Focal Plane Mask and Lyot Stop with ribs fabricated with deep reactive ion etching of an SOI wafer. The thinner device side of the wafer is typically 25 microns thick and is coated with aluminum to achieve the required opacity. The images are not to scale with each other.

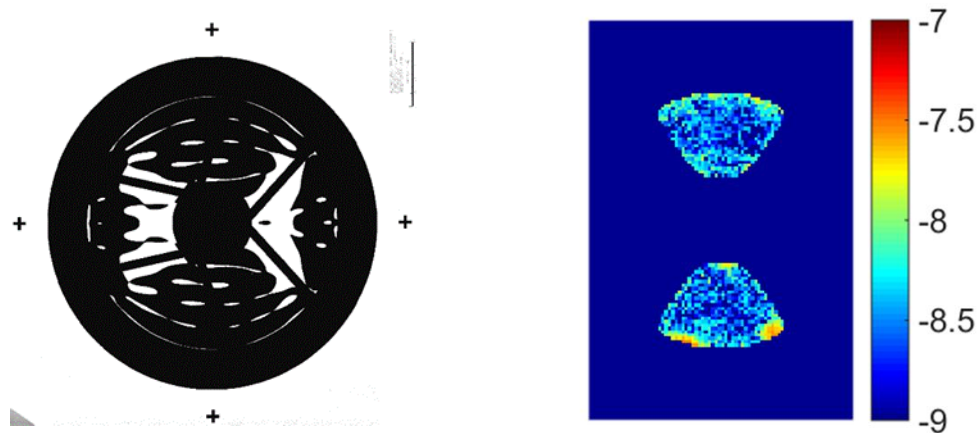
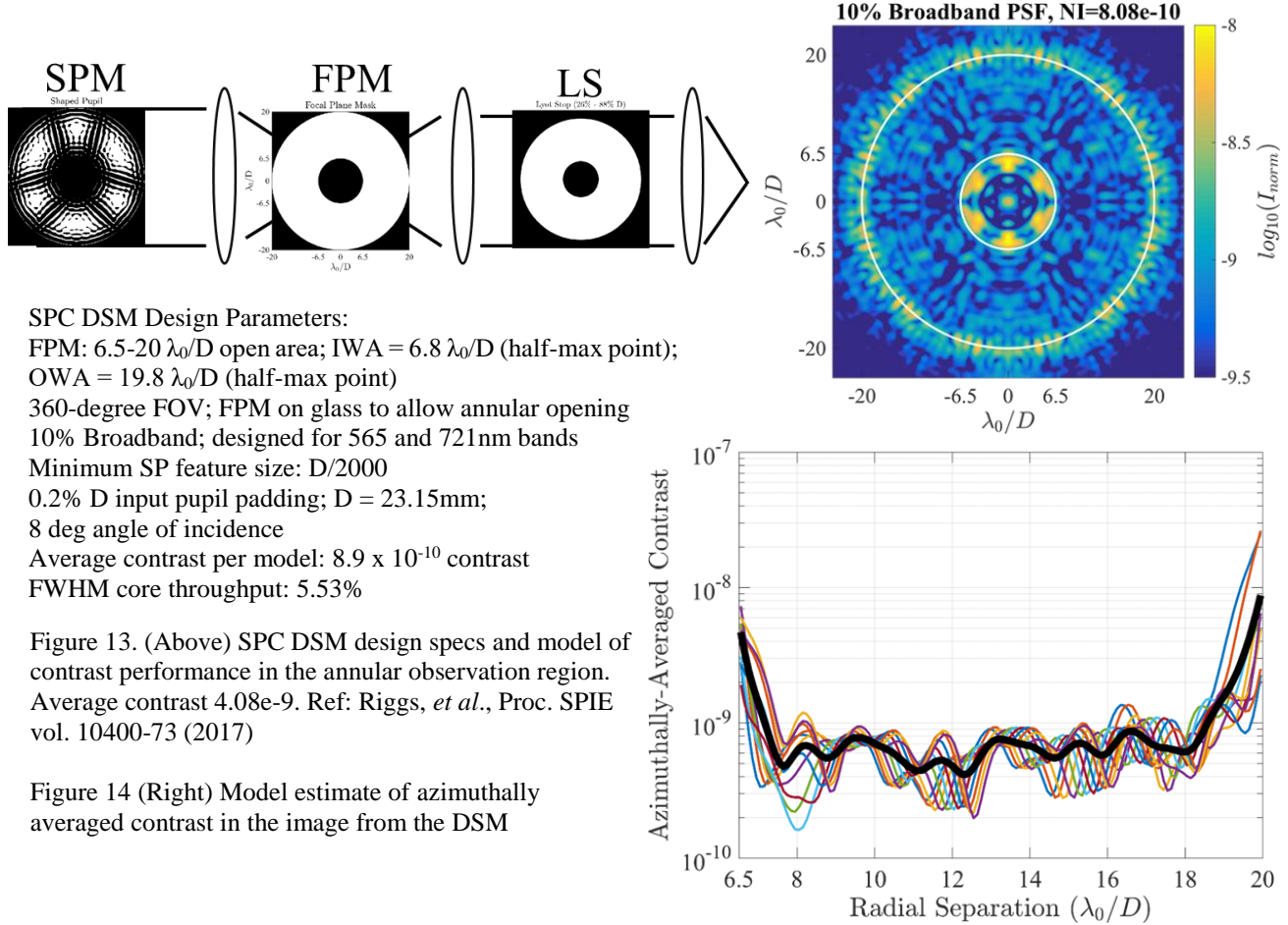


Figure 12. Testbed Milestone demonstration of SPC performance. Left: Mask employed in the testbed. Right: Dark hole contrast (log scale) demonstration in static environment with 60nm spectral band centered at 550nm. Average contrast  $4.08 \times 10^{-9}$ . Ref: Cady, *et al.*, Proc. SPIE vol. 10400-14 (2017)

### SPC Disk Science Mask (DSM)

For disk science observations over a  $360^\circ$  annual region, a new binary amplitude shaped pupil mask optimized with a  $2000 \times 2000$  grid with corresponding annular focal plane mask open from  $6.5$ - $20 \lambda/D$  and Lyot stop open from  $26\%$ - $88\%$  of the pupil diameter were designed recently for laboratory testing and performance demonstration. The concept design, specs and model predictions are shown in figures 13 and 14.



The SPC DSM with  $2k \times 2k$  pixels design was fabricated with black silicon and aluminum with the same process adopted for the characterization mask as described in sections 2 and 3 above. However, the Focal Plane Mask was fabricated on a  $25$  mm diameter double side AR coated fused silica substrate to allow for annular  $360^\circ$  field of view for disk science observation. The fabricated Disk Science Mask and Focal Plane Mask installed in the testbed in June 2017 are shown in figures 15 and 16. The FPM contains 6 annular ring masks and two pin holes for calibration (not observable in the figure) on either side of the large circle. The annular ring masks are designed with different dimensions for different observation areas and wavelengths. The image imperfections are a result of the illuminations differences and stitching artifacts of the composite image containing 130 sub images.

### Defects on fabricated SPC Disc Science Mask

Detailed microscopic observation revealed a few defects in the aluminum areas as well as in the black silicon areas. These were imaged and characterized with size and location. A total of 11 significant defects were observed and identified some of which are shown in figure 17. Four of these defects were larger than  $1000$  sq microns in area. Hence model based analysis of the impact on performance was performed.



Figure 15. SPC Disk Science Mask installed in the testbed on 06/29/2017 along with new focal plane mask.

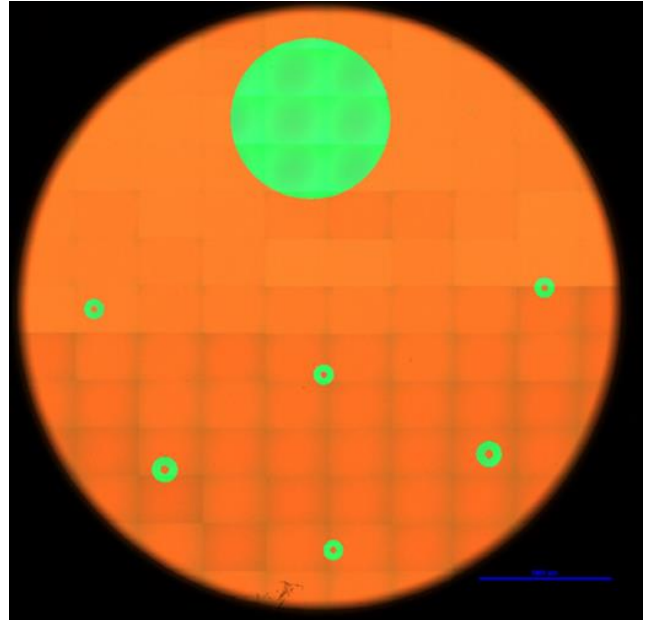


Figure 16. Composite microscope image of the Disk Science focal plane mask on AR coated glass installed in the testbed. Image stitching artifacts are seen.

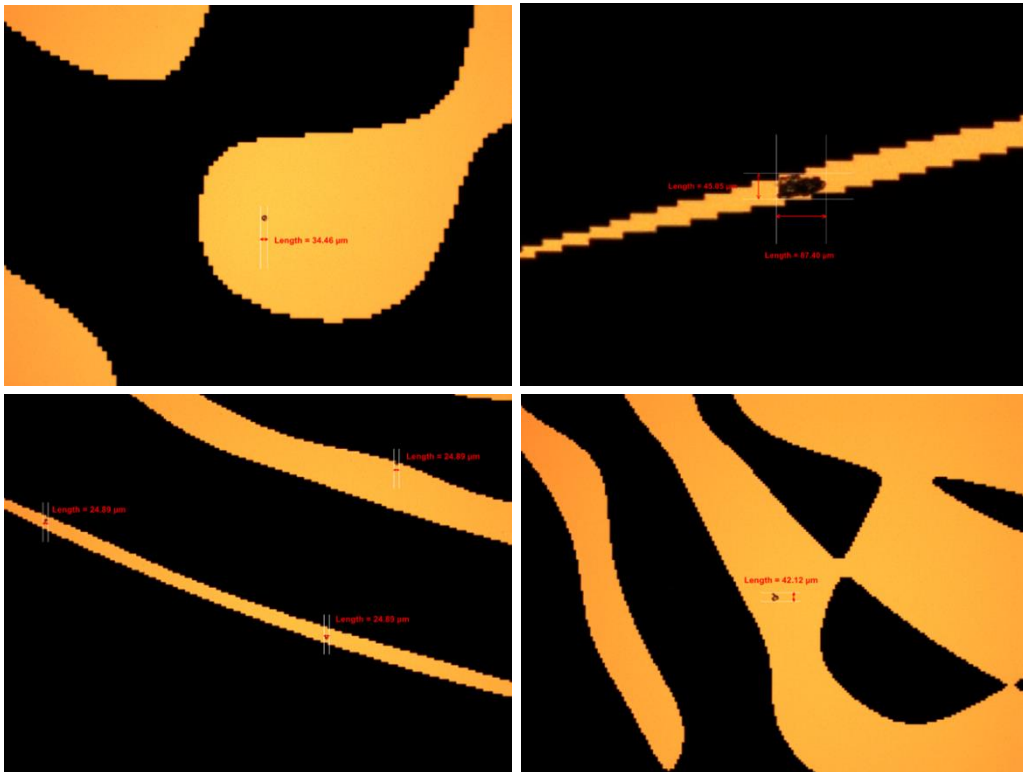


Figure 17. A few of the defects seen on the shaped pupil DSM mask installed in the testbed.



## Performance impact due to defects

Model based analysis was performed on the impact from two of the largest defects as shown in figure 18. The defects were assumed to be purely amplitude aberrations. The areas of the defects were approximately 20 pixels for Defect A and 10 pixels for Defect B. Open-loop simulations show Defects A and B have virtually no effect on the achievable raw contrast. The azimuthally averaged raw contrast with and without the two defects is plotted in figure 19. A second model analysis was performed with 100 other smaller  $10\mu\text{m} \times 10\mu\text{m}$  size defects at random in addition to the large defects A and B. The plot on figure 20 shows that the effect on raw contrast is still negligible. Testbed results to be derived soon will include testbed related aberrations and misalignments. Further details of such analysis can be found in a companion paper (Riggs, *et al.*, Proc. SPIE Vol. 10400-73 (2017)).

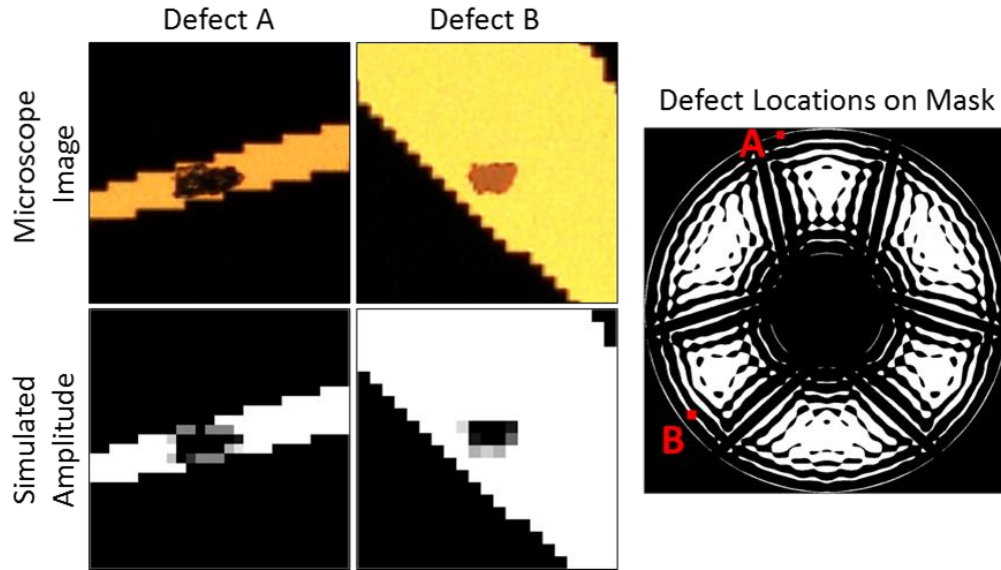


Figure 18. Two of the largest defects and their locations on the DSM mask for detailed modeling.

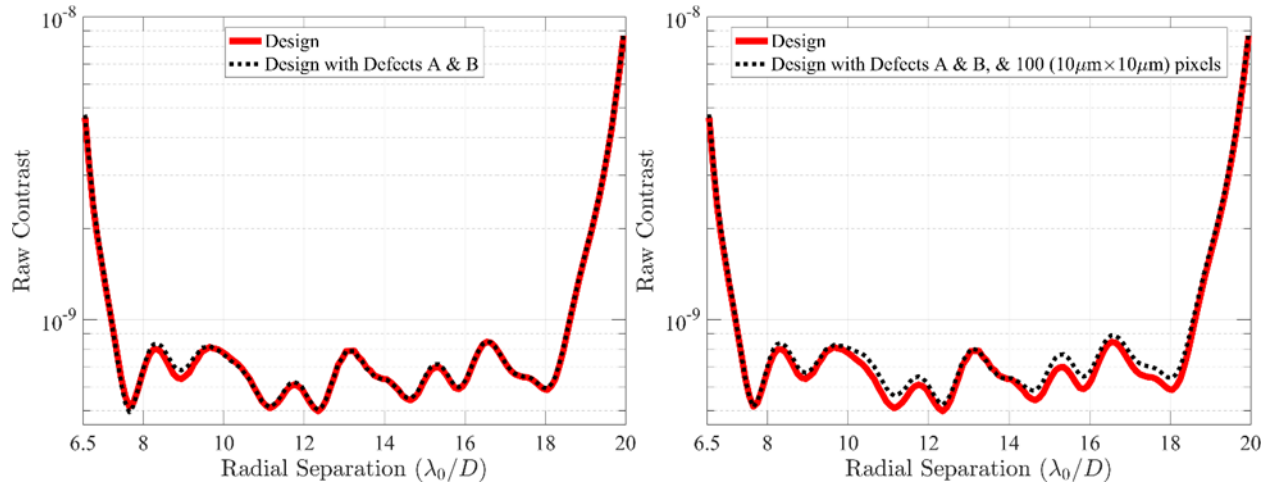


Figure 19 (Above Left): Model based analysis of the impact of the two large defects seen in Figure 18. Azimuthally averaged raw contrast in the annular dark hole region shown in figure 13.

Figure 20 (Above Right): Model based analysis of the impact of the two large defects along with 100 other  $10\mu\text{m} \times 10\mu\text{m}$  size defects.

Surface flatness and reflectivity of the fabricated DSM

Other criteria to pick the best DSM mask out of the 9 samples made in June 2017 include the surface flatness and reflectivity of the masks in addition to defect mapping. Figure 21 shows the Zygo interferometer measurement of the surface flatness of the best fabricated mask sample #25-3 that was chosen to be the best among them and was installed in the testbed for further testing. The rms surface figure is less than 0.03 wave or 19nm when piston, tilt and power terms are removed. The noisy data and the consequent high pv value are due to the extreme reflectivity variations and the depth associated with black silicon structure vs the aluminum areas as seen in the SEM image in figure 10.

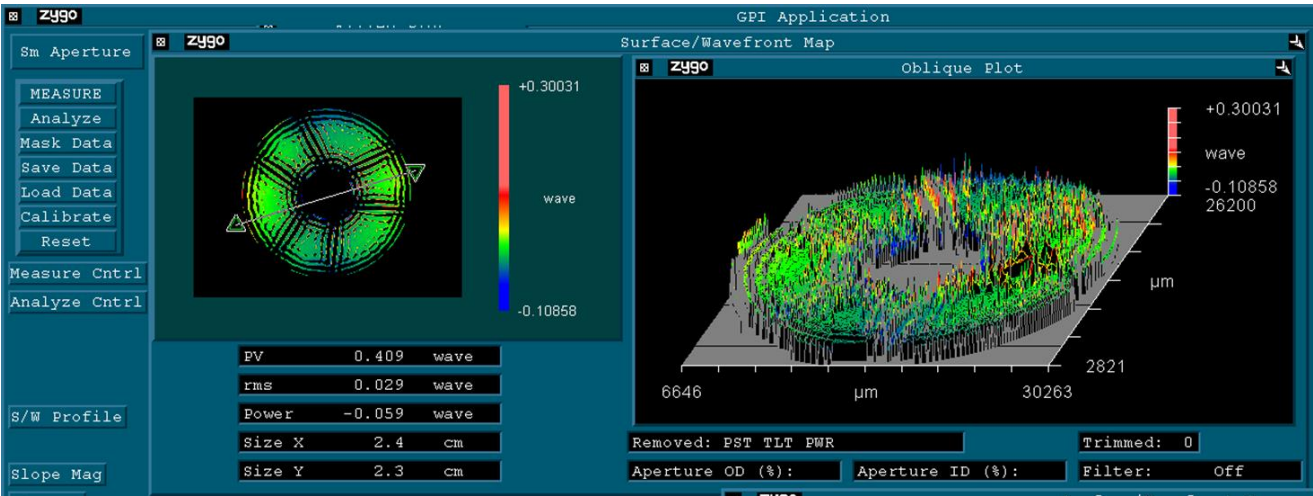


Figure 21. Zygo interferometer map of the DSM mask surface. The noisy nature of the surface and the consequent high pv value are due to the extreme reflectivity variations and the depth associated with black silicon structure vs the aluminum areas as seen on the SEM images in figure 10.

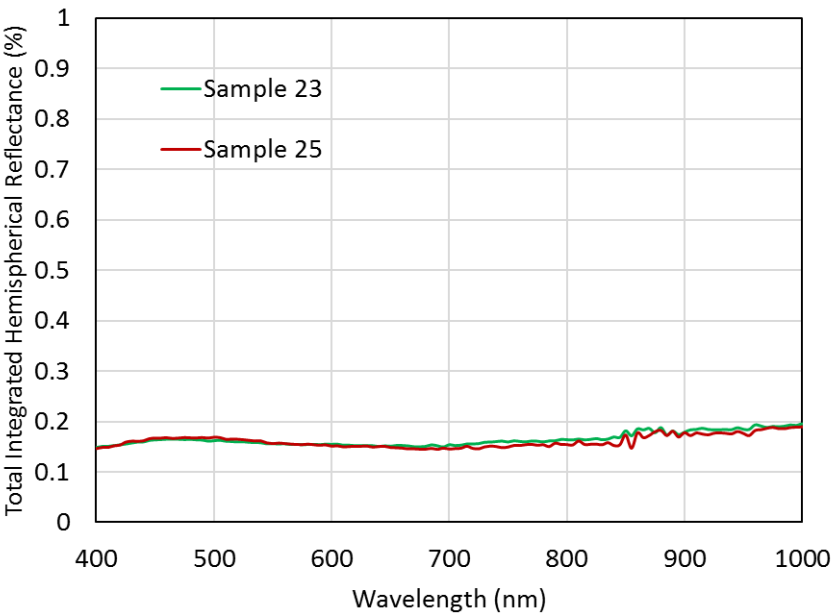


Figure 22. Total hemispherical reflectivity of black silicon samples fabricated as witnesses to mask samples #23 and #25.

The specular reflectivity of the aluminum and black silicon of the chosen sample were measured using a HeNe laser based test station as described in our earlier paper in 2016 (JATIS Vol. 2. No.1, Jan-March 2016 pp 011005-1-16). The Al region

reflectivity was measured to be 90.1% at 633nm and the black silicon reflectivity was measured to be  $8.3 \times 10^{-8}$ . The diffuse hemispherical reflectivity was measured on the large black circles from the same silicon substrate with a Perkin Elmer 1050 spectrophotometer fitted with an integrating sphere. Figure 22 shows the measured hemispherical reflectance from two samples of the same batch made in June 2017.

#### 4. HYBRID LYOT CORONAGRAPH (HLC) MASKS

Hybrid Lyot coronagraph masks that enable 360 deg observation around the star image are designed (Trauger et al., 2016) with a profiled dielectric layer on a metal dot on an anti reflection coated glass substrate for transmission. Fabrication of these masks involves gray scale lithography with a polymethyl glutarimide (PMGI) photoresist that serves as the transparent dielectric. Nickel with chosen thickness for the required optical density is used as the metal dot below the PMGI layer. A phase dimple to provide  $\pi/2$  radian phase shift on reflection is incorporated at the center of the mask to provide the necessary signal for the Zernike low order wavefront sensor and corrector in the system.

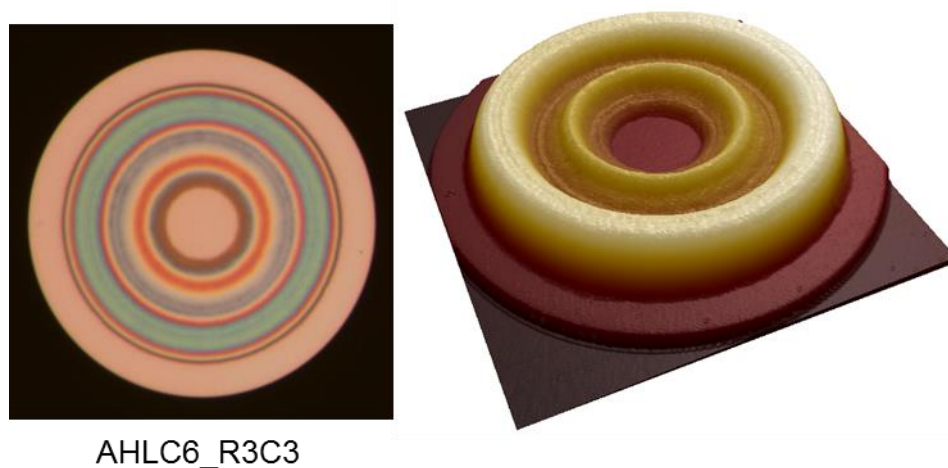


Figure 23. Left: Optical microscope image of the HLC mask with phase dimple. Right: Atomic Force Microscope (AFM) image of the same.

The structure of such a mask that has been employed for milestone demonstrations in JPL high contrast imaging testbed (HCIT) is shown in figure 23. Coronagraph mean contrast accomplished over a 10% band at 550nm is shown in figure 24. For details of the test methodologies and results, refer to Seo, *et al.*, (2016, 2017), and Shi, *et al.*, (2016, 2017).

##### Azimuthally varying HLC mask

Optimization of the HLC mask design to improve contrast and throughput is pursued for further iterations. One such optimized azimuthally varying HLC mask design is shown in figure 25. The HLC mask fabrication involves a two-step grayscale electron-beam lithography (EBL) process with a polymethyl glutarimide (PMGI, Ref: 12, Microchem) resist that serves as the transparent dielectric. The nickel dots are fabricated by first e-beam patterning a positive-tone resist layer to open circles for the nickel dots and cross marks near the edge of the wafer for alignment of the

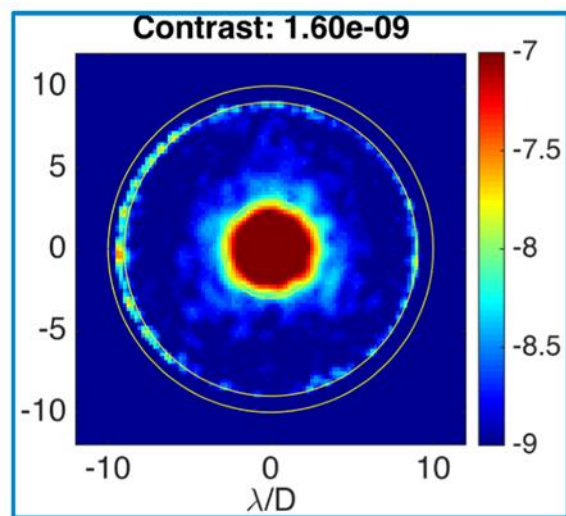


Figure 24. Best HLC Static Contrast (10% BW at 550nm); Ref: Seo, et al., Proc. SPIE 10400-15, 2017.

PMGI e-beam exposure. Next, the occulting metal layer stack (~5 nm of titanium for adhesion and ~100 nm of nickel) is e-beam evaporated over the entire substrate. The substrate is then soaked in a solvent bath that dissolves the e-beam resist, lifting off all of the Ti/Ni except for the desired dots and crosses. Next, the substrate with metal patterns is spin-coated with a PMGI layer thicker than the desired dielectric profile, and a thin layer of chromium is evaporated to serve as a conductive layer for the grayscale e-beam lithography. The desired grayscale dielectric profile is provided as pixel pattern of thicknesses and is converted to a grayscale e-beam dose pattern using JPL in-house software [Wilson, et al., 2005]. The e-beam patterns are exposed using JPL's JEOL 9500FS electron-beam lithography system. The nickel crosses are used as marks for the tool's automated layer-to-layer alignment routine. Finally, the chromium discharge layer is etched off, and the PMGI is developed iteratively [Wilson, et al., 2005] until the height of grayscale profile best matches the design as measured by atomic force microscopy. Figure 26 shows the AFM image of one of these azimuthally varying masks recently fabricated in MDL and installed in the testbed for detailed tests. Detailed analysis of the accuracy of the fabricated mask is underway and the results will be used to improve subsequent iterations. Testbed results will provide the necessary feedback for further optimization of designs.

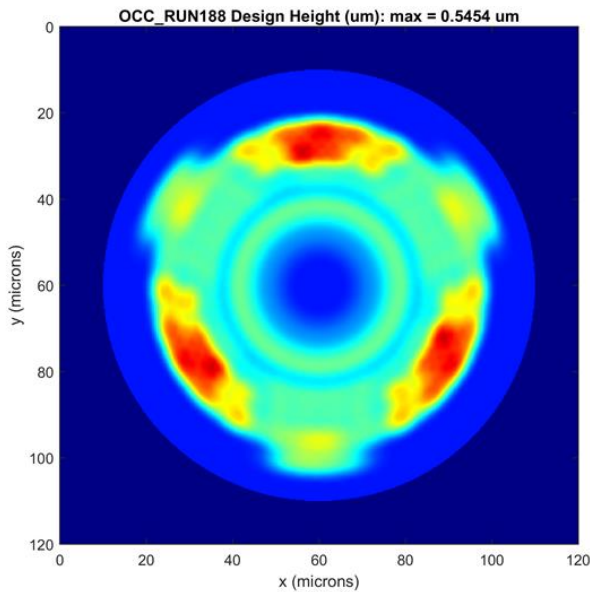


Figure 25. Azimuthally varying HLC mask design

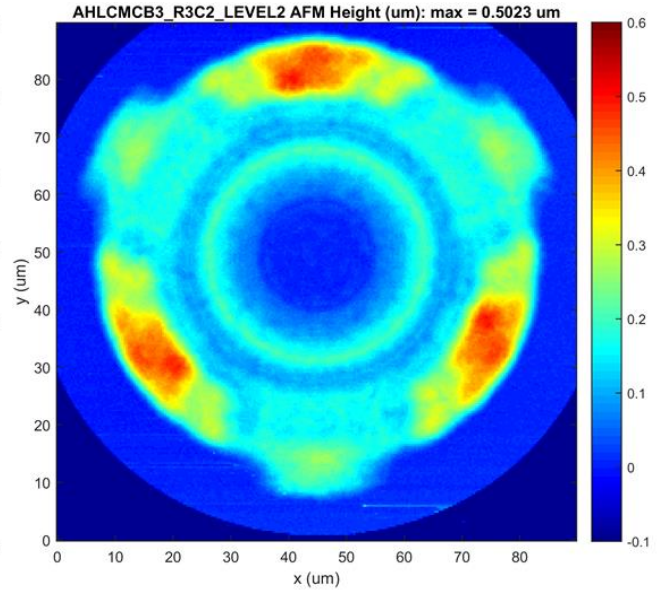


Figure 26. AFM image of fabricated AHLC mask

## 5. LABORATORY SCALE STAR SHADE MASKS

### Scaled Down Miniature Version of Star Shade Masks

A space borne star shade occulter designed to suppress the host star light reaching the telescope is typically very large (30 to 75 m in diameter) and will be flown far (30,000 to 150,000 km) from the telescope. Hence full scale practical tests in the lab are not feasible. However, scaled down versions of the star shade can be designed with flight-like Fresnel number and tested. A laboratory testbed has been set up at Princeton University for validating the physical principles and to verify performance against models (Galvin et al., 2016, Sirbu et al., 2016, Harness et al., 2017). Designs optimized by the Princeton University team are being fabricated at the Micro Devices Lab (MDL) in JPL. A representative photograph of a recently fabricated 50mm diameter star shade mask is shown in figure 27. The mask made with electron-beam lithography (EBL) and Deep Reactive Ion Etching (DRIE) on an SOI wafer with a thin SiN<sub>x</sub> membrane defining the edges has 16 precisely shaped petals with ~0.5μm edge accuracy. Tip to tip length of each petal is 16 mm. The inner tip width is 7.54μm and the outer tip width is 22.12μm. Microscopic image of two of the petals is shown in figure 28. Finer details of the edges are imaged with higher resolution objectives and scanning electron microscope (SEM) as shown in figure 29 for detailed modeling and analysis.



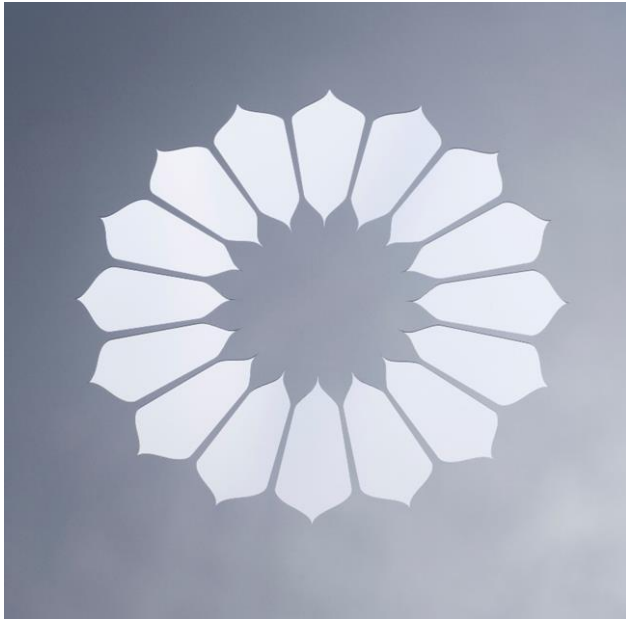


Figure 27. Photograph of a star shade mask fabricated by e-beam lithography and deep reactive ion etching on an SOI wafer with SiNx membrane.

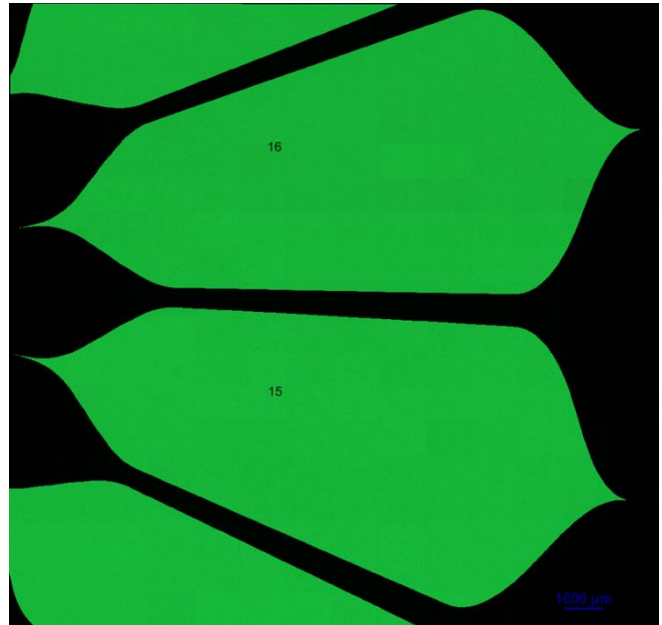


Figure 28. High resolution optical microscope image of two of the petals of the mask.

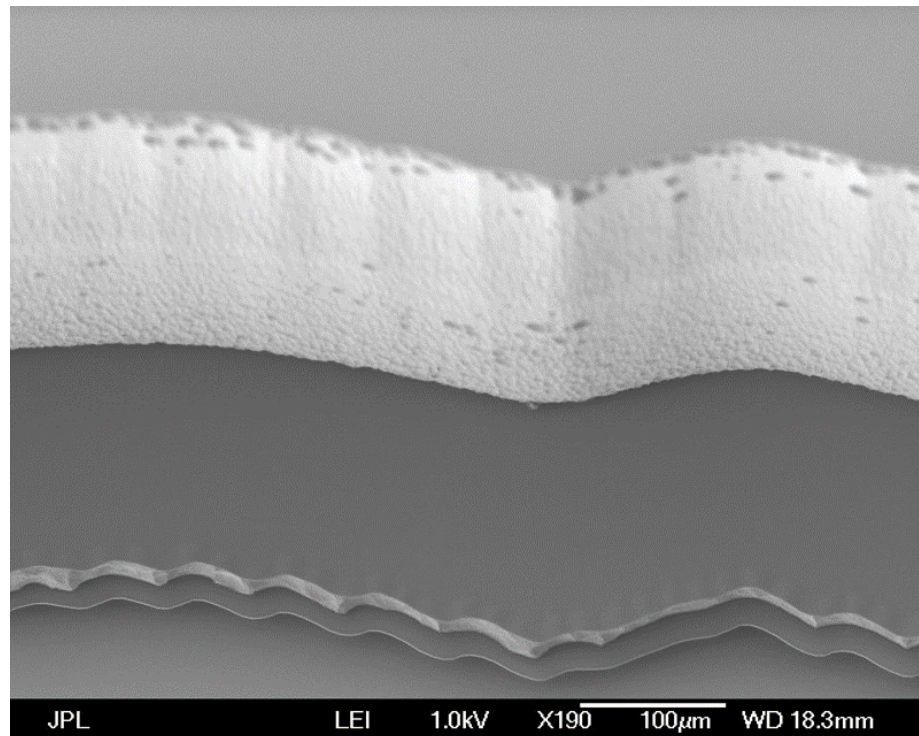


Figure 29. High resolution scanning electron microscope (SEM) image of a petal edge showing the thin membrane defining the edge shape to  $\sim 0.25$  micron accuracy. The recessed ledge at the backside is also seen clearly.

### Identification and quantification of defects

Defects and imperfections on the star shade mask contribute to excess scattered light into the image plane causing contrast degradation. Precise identification of defects help with performance modeling as well as to match with image signatures observed on the testbed. High resolution microscope images with 50x or 100x objectives provide the necessary details as shown in figures 30 and 31.

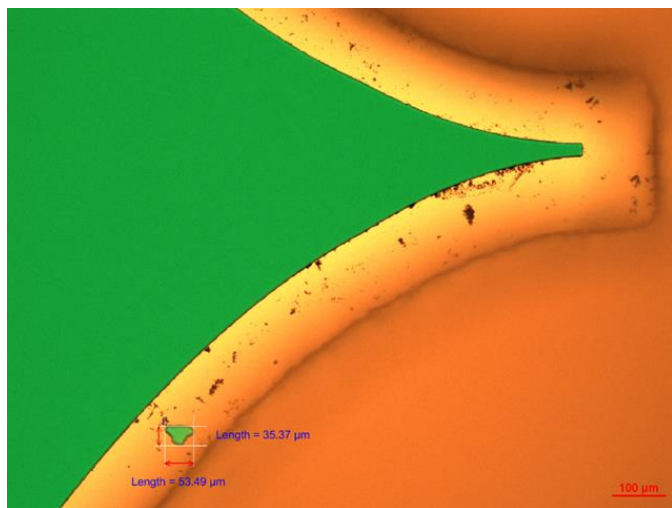


Figure 30. High resolution optical microscope image from the back side (Reflection (yellow) + Transmission (green)) of a  $\sim 35\mu\text{m} \times 53\mu\text{m}$  pin hole near a petal edge on the mask.

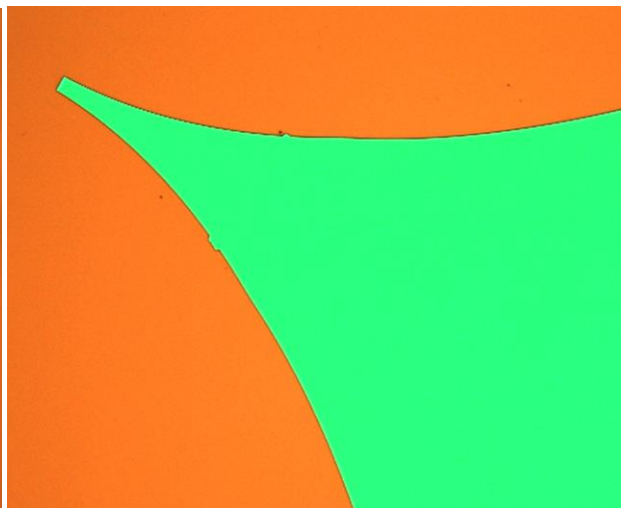


Figure 31. High resolution optical microscope image from the front side (Reflection (yellow) + Transmission (green)) of small over-etched spots on a petal edge on the mask.

### Nature of defects and performance impact

The defects observed on the fabricated star shade masks can be classified as a) systematic and b) random. Systematic defects occur primarily due to lithographic bias during resist exposure when employing optical contact lithography from an electron beam patterned glass master causing the edges wider than intended. For example, the outer tip of the petal which is expected to be  $22.12\mu\text{m}$  wide sometimes becomes  $23\mu\text{m}$ . Direct electron lithography on the wafer can result in much tighter dimensional accuracy as we obtained in our latest mask with such over-etch error less than  $0.25\mu\text{m}$ . Random errors occur due to variety of other reasons related to chemical and ion based etching processes. Pin holes and edge defects occur as shown in figures 30 and 31. The pin hole shown in figure 30 is particularly large ( $\sim 35\mu\text{m} \times 53\mu\text{m}$ ) which can impact the contrast significantly. Detailed modeling and testbed results with this mask are discussed in another paper of Harness, *et al.*, 2017.

## 6. SUMMARY AND CONCLUSIONS

- HLC and SPC masks for discovery and spectroscopy of exoplanets with WFIRST telescope have been designed and fabricated successfully at JPL with several milestone demonstrations paving the way to produce flight components.
- Similarly, laboratory scale star-shade masks have been fabricated at JPL for testbed experiments at Princeton University; improvements in fabrication process are in progress to minimize defects and to tighten mask edge accuracy to better than  $0.5\mu\text{m}$ .
- Future exoplanet focused mission concepts such as HabEx and LUVOIR need more advanced masks to reach deeper contrast levels over wider bandwidth and to handle potentially segmented telescope apertures. Further research in mask design and fabrication will be continued to accomplish these goals.

## 7. ACKNOWLEDGEMENTS

This work was performed at the Jet Propulsion Laboratory, California Institute of Technology, under a contract with the National Aeronautics and Space Administration. The authors thank the Princeton University High Contrast Imaging Lab team under Prof. N. J. Kasdin for their support with the design of SPC and Star Shade Masks over several years. They also acknowledge the support of the JPL WFIRST CGI management and other team members, particularly Dwight Moody and John Trauger for the design updates of HLC masks. Reference herein to any specific commercial product, process, or service by trade name, trademark, manufacturer, or otherwise, does not constitute or imply its endorsement by the United States Government or the Jet Propulsion Laboratory, California Institute of Technology.

## 8. REFERENCES

- [1] Balasubramanian, K., V. White, K. Yee, P. Echternach, R. Muller, M. Dickie, E. Cady, C. M. Prada, D. Ryan, I. Poberezhskiy, B. Kern, H. Zhou, J. Krist, B. Nemati, A.J. E. Riggs, N.T. Zimmerman, and N. J. Kasdin, "WFIRST-AFTA coronagraph shaped pupil masks: design, fabrication, and characterization", *J. of Astronomical Telescopes, Instruments and Systems* 2(1), 011005, Jan-Mar (2016).
- [2] Balasubramanian, K., D. Wilson, V. White, R. Muller, M. Dickie, K. Yee, R. Ruiz, S. Shaklan, E. Cady, B. Kern, R. Belikov, O. Guyon, and N. J. Kasdin, "High contrast internal and external coronagraph masks produced by various techniques," *Proc. SPIE Vol. 8864*, pp. 88641R 1-9, (2013).
- [3] Cady, E., *et al.*, "Progress on the occulter experiment at Princeton", *Proc. SPIE vol. 7440*, (2009).
- [4] Cady, E., C. M. Prada, X. An, K. Balasubramanian, R. Diaz, N. J. Kasdin, B. Kern, A. Kuhnert, B. Nemati, I. Poberezhskiy, A. J. Eldorado Riggs, R. Zimmer, and N. Zimmerman, "Demonstration of high contrast with an obscured aperture with the WFIRST-AFTA shaped pupil coronagraph", *Journal of Astronomical Telescopes, Instruments, and Systems*, 2(1):011004, January (2016).
- [5] Cady, E., K. Balasubramanian, J. Gersh-Range, N. J. Kasdin, B. Kern, R. Lam, C. M. Prada, D. Moody, K. Patterson, I. Poberezhskiy, A.J.E. Riggs, B.-J. Seo, F. Shi, H. Tang, J. Trauger, H. Zhou, and N. Zimmerman, "Shaped pupil coronagraphy for WFIRST: high-contrast broadband testbed demonstration", *Proc. SPIE 10400-14* (2017).
- [6] Cash, W., "Detection of Earth-like planets around nearby stars using a petal-shaped occulter," *Nature* 442, pp. 51-53, July (2006).
- [7] Crill, B., and N. Siegler, "Exoplanet Exploration Program Technology Plan Appendix: 2017," Jet Propulsion Laboratory Publications JPL Document No. D-98883, (2017).  
<https://exoplanets.nasa.gov/exep/technology/technology-overview>
- [8] Crill, B., and N. Siegler, "Space Technology for Directly Imaging and Characterizing Exo-Earths", *Proc. SPIE Vol. 10398* (2017).
- [9] Galvin, M., Y. Kim, N. J. Kasdin, D. Sirbu, R. Vanderbei, D. Echeverri, G. Sagolla, A. Rousing, K. Balasubramanian, D. Ryan, S. Shaklan, and D. Lisman, "Design and Construction of a 76m Long-Travel Laser Enclosure for a Space Occulter Testbed", *Proc. of SPIE Vol. 9912*, 99126N-1 (2016).
- [10] Groff, T.D., C. M. Prada, E. Cady, M. Rizzo, A. Mandell, Q. Gong, M. McElwain, N. Zimmerman, P. Saxena, O. Guyon, "Wavefront control methods for high-contrast integral field spectroscopy", *Proc. SPIE 10400-24* (2017).
- [11] Harness, A., S. Shaklan, P. Dumont, Y. Kim, and N.J. Kasdin, "Modeling and performance predictions for the Princeton Starshade Testbed", *Proc. SPIE Vol. 10400*, (2017).
- [12] [http://www.microchem.com/Prod-PMGI\\_LOR.htm](http://www.microchem.com/Prod-PMGI_LOR.htm)
- [13] Kim, Y., Galvin, M., Kasdin, N.J., Vanderbei, R., Ryu, D., Kim, K., Kim, S., Sirbu, D., "Design of a laboratory testbed for external occulters at flight Fresnel numbers," *Proc. SPIE 9605*, 960511 (2015).
- [14] Krist, J., B. Nemati, and B. Menneson, "Numerical modeling of the proposed WFIRST-AFTA coronagraphs and their predicted performance", *Journal of Astronomical Telescopes, Instruments, and Systems*, 2(1):011003, January (2016).
- [15] Riggs, A.J.E., N. Zimmerman, B. Nemati, J. Krist, "Shaped pupil coronagraph design improvements for the WFIRST CGI", *Proc. SPIE Vol. 10400-73* (2017).
- [16] Seo, B.-J., B. Gordon, B. Kern, A. Kuhnert, D. Moody, R. Muller, I. Poberezhskiy, J. Trauger, and D. Wilson, "Hybrid Lyot coronagraph for wide field infrared survey telescope-astronomy focused telescope assets: occulter fabrication and high contrast narrowband testbed demonstration", *Journal of Astronomical Telescopes, Instruments, and Systems*, 2(1):011019, January (2016).

- [17] Seo, B.-J., E. Cady, B. Gordon, B. Kern, R. Lam, D. Marx, D. Moody, R. Muller, K. Patterson, C. Prada, I. Poberezhskiy, E. Sidick, F. Shi, J. Trauger, and D. Wilson, "Hybrid Lyot Coronagraph for WFIRST: High Contrast Broadband Testbed Demonstration", Proc. SPIE 10400-15 (2017).
- [18] Shi, F., K. Balasubramanian, R. Hein, R. Lam, D. Moore, J. Moore, K. Patterson, I. Poberezhskiy, J. Shields, E. Sidick, H. Tang, T. Truong, J. K. Wallace, X. Wang, and D. Wilson, "Low-order wavefront sensing and control for WFIRST-AFTA", J. of Astronomical Telescopes, Instruments and Systems 2(1), 011021, Jan-Mar (2016).
- [19] Shi, F., E. Cady, B.-J. Seo, X. An, K. Balasubramanian, B. Kern, R. Lam, C. Mejia Prada, D. Moody, K. Patterson, I. Poberezhskiy, J. Shields, E. Sidick, H. Tang, J. Trauger, T. Truong, V. White, D. Wilson, and H. Zhou, "Dynamic Testbed Demonstration of WFIRST Coronagraph Low Order Wavefront Sensing and Control (LOWFS/C)", Proc. SPIE 10400-13 (2017).
- [20] Sirbu, D., N. J. Kasdin, R. Vanderbei, "Diffraction-based analysis of tunnel size for a scaled external occulter testbed," Proc. SPIE 9904, (2016).
- [21] Trauger, J., D. Moody, J. Krist, and B. Gordon, "Hybrid Lyot coronagraph for WFIRST-AFTA: coronagraph design and performance metrics", J. of Astronomical Telescopes, Instruments and Systems 2(1), 011013, Jan-Mar (2016).
- [22] Wilson, D.W., Richard E. Muller, Pierre M. Echternach, Johan P. Backlund, "Electron-beam lithography for micro- and nano-optical applications," Proc. SPIE 5720, Micromachining Technology for Micro-Optics and Nano-Optics III, 68, April 11, (2005).
- [23] Yee, K., V. White, K. Balasubramanian, D. Ryan, "Ultra Low Reflectivity Black Silicon Surfaces and Devices Enable Unique Optical Applications", Proc. SPIE 104354-31 (2017).
- [24] Zimmerman, N. T., A. J. Eldorado Riggs, N. Jeremy Kasdin, Alexis Carlotti, Robert J. Vanderbei, "Shaped pupil Lyot coronagraphs: high-contrast solutions for restricted focal planes", J. Astron. Telesc. Instrum. Syst; 2(1):011012. doi: 10.1117/1.JATIS.2.1.011012, (2016).